

AEROBIC ENVIRONMENTS ON MARS

Vlada Stamenković, Lewis M. Ward, Michael Mischna, & Woodward W. Fischer. “Aerobic Environments on Mars.” Nature, submitted.

Aerobic respiration is the most widespread and energetically favorable metabolism on Earth; it enabled complex multicellularity¹. The history of O₂ and aerobic respiration on the Earth is tied to that of photosynthesis², resulting today in ~21 vol.% O₂ in an ~1 bar atmosphere. In contrast, modern Mars has a thin, ~6 mbar atmosphere with O₂ produced photochemically from CO₂ and H₂O, and hydrogen escape³. Despite the thin atmosphere and overall cold climate, liquid water and brines can exist at and near the surface^{4,6}. In particular, Ca- and Mg-perchlorate brines can remain a “normal” liquid above ~200 K and a supercooled liquid down to 140-150 K^{7,8}. Using new solutions that describe the solubility of molecular oxygen (O₂) in these and other liquids, we show that, today, all of Mars can host liquid surface environments with sufficient dissolved O₂, [O₂]_{aq}, to support aerobic microorganisms, with concentrations that vary substantially with location. Closer to the equator, intermediate [O₂]_{aq} values of 10⁻⁴-10⁻³ mol m⁻³ can exist. The highest [O₂]_{aq} values of 10⁻³-10⁻¹ O₂ mol m⁻³ are feasible in cold polar regions—these values are high enough to support respiration by some multicellular basal animals⁹. Such aerobic oases cover ~6.5% of the Martian surface today, but decrease at higher obliquity, or axial tilt, becoming unlikely above ~50°. Our results illustrate that today, and for the

geologically recent past, Mars could have had environments with sufficient levels of dissolved O₂ to support aerobic biology, were it present.

The geologic record of Mars provides evidence of ancient aqueous environments on or near the surface and evidence of great environmental change¹⁰ likely driven by variations in obliquity¹¹ and atmospheric loss processes¹². While these observations support the idea that Mars was habitable¹³, we don't know if it was ever inhabited; and if so, what metabolisms might have been, or might still be, available to support life.

Recent evidence demonstrates hydrated magnesium and calcium perchlorate salts at various locations on Mars^{5,6,14}, which indicate the existence of Mg(ClO₄)₂-Ca(ClO₄)₂-H₂O brines, and are, in some cases, associated with seasonal flow structures like the modern recurring slope lineae^{4,5} (RSL). Ca- and Mg-perchlorate brines exhibit a much lower freezing point than pure water, by 60-80 K^{7,8}; and, for the eutectic composition, they effectively supercool down to 140-150 K before transitioning into a glass, even when mixed with Martian regolith simulant⁷. Also, theoretical calculations¹⁵ and experiments⁷ using brines containing Martian soils with perchlorates (e.g., Phoenix soil analog¹⁵) show that dissolved perchlorate concentrations can readily reach eutectic concentrations during freezing.

Little attention has been given to the possibility of aerobic respiration on Mars due to the scarcity of O₂ in the Martian atmosphere^{3,16}. However, geochemical evidence from Martian meteorites¹⁷ and manganese-rich rocks¹⁸⁻²⁰ point to highly oxidizing aqueous environments on Mars in its past, suggesting that O₂ played a role in chemical weathering

of Mars crust. Meanwhile, recent experiments, observation, and calculations have lowered the known $[O_2]_{aq}$ limits for aerobic respiration to $\sim 10^{-6}$ mol m⁻³ in microorganisms²¹ and $\sim 2 \cdot 10^{-3}$ mol m⁻³ in sponges⁹. Understanding the solubility of O₂ in liquid brines, especially containing Ca- and Mg-perchlorates, under Martian conditions is needed to evaluate the spatial and temporal distribution of aerobic environments on Mars.

To achieve this, we developed a new comprehensive thermodynamic framework applicable to Martian conditions that calculates the solubility of O₂ in liquid brines composed of water and salts, such as perchlorates (Ca(ClO₄)₂, Mg(ClO₄)₂, NaClO₄), chlorides (MgCl₂, NaCl), and sulfates (MgSO₄). We coupled this solubility framework to a Mars general circulation model (GCM) to compute the solubility of O₂ as a function of annually averaged values of pressure and temperature varying with location on the Martian surface today (for obliquity $\sim 25^\circ$) and for other values of the planet's obliquity²² (10°, 15°, 20°, 40°, 60°, 90°). This gives us 3D maps of oxygen solubilities – representing the local, climatically-induced potential for the formation of oxygen-rich brines on Mars for different obliquities. Finally, we used calculations of Mars' obliquity changes in the past ~ 20 Ma and the next ~ 10 Myr²³ as input for the GCM to infer how O₂ solubility in surface environments varies across time.

The fundamental challenge was to describe gas dissolution processes in brines below the freezing point of water. To calculate the solubility of O₂ in these liquids, we first computed how the solubility of O₂ changes as a function of temperature in supercooled water. The only uncertainty for this computation concerns the specific heat of dissolved O₂ in supercooled water. For this, we compared a conservative estimate assuming a constant

value (BE, best estimate, in Figures 1-3), tested plausible alternatives resulting from the behavior of the specific heat of supercooled water²⁴ and brines^{24,25} (which led to no significant differences from BE), and derived an unreachable thermodynamic lower limit for the solubility of O₂ (worst case, WC, in Figures 1-3). The presence of dissolved cations and anions (for Ca(ClO₄)₂, Ca²⁺ and ClO₄⁻) reduces the solubility of O₂ in water²⁶. To account for this “salting out”²⁷ of O₂, we applied the Pitzer approach²⁸, incorporating O₂-cation, O₂-anion, and O₂-cation-anion electrostatic interactions, and estimated their temperature dependence with the apparent volume model²⁹ and available experimental data. The BE model results agree well (generally within a few percent) with existing data.

We examined the solubility of O₂ for various potential Martian brines as a function of temperature from 140-300 K for an average Mars surface pressure of ~6.1 mbar, assuming, for each temperature, the critical minimum concentration of salt needed for the brine to remain liquid (Figure 1a). Only Mg- and Ca-perchlorates have been experimentally shown to remain liquid in a supercooled state far below their eutectic temperature to at least ~140-150 K⁷ (Figure 1b), and, hence, only for those brines do solubilities increase by at least five orders of magnitude from 273-140 K for BE (Figure 1c). For WC, the O₂ solubilities at 140 K for Ca- and Mg-perchlorates are reduced in comparison to BE but the O₂ solubility still increases by about two orders of magnitude from 273-140 K. All other salts can be only slightly supercooled below their eutectic temperature (Figure 1b), leading to solubilities of O₂ varying by less than one order of magnitude for Martian temperature and average pressure conditions. Over all the solution space, dissolved O₂ concentrations

are in excess of—and commonly orders of magnitude higher than $\sim 10^{-6}$ mol m⁻³ (Figure 1c, d).

O₂ solubility is primarily controlled by temperature but also by pressure—both of which vary substantially across Mars' surface. To assess spatial variation in dissolved O₂ concentrations, we connected our O₂ solubility model for Ca- and Mg-perchlorate brines with a climate model for modern-day Mars, which accounts for a perennial south polar cap of CO₂ (SPC)²². For each temperature, we computed the critical concentration of Ca(ClO₄)₂ or Mg(ClO₄)₂ needed for the brine to remain liquid, and then solved for $[O_2]_{aq}$ under scenarios with and without supercooling of these brines. We observed large gradients in $[O_2]_{aq}$ values across the Martian surface, with polar regions having the potential to harbor fluids that contain up to 0.2 mol m⁻³ O₂, and the least O₂-rich environments at about $\sim 2.5 \cdot 10^{-5}$ mol m⁻³ O₂. Without supercooling, liquid perchlorate brines should occur primarily at latitudes below 50°, leading to differences in potential solubility of ~ 1 order of magnitude depending on location in this belt (see Figure 2b). Even for WC (with and without supercooling), values for the solubility of O₂ in Ca- and Mg-perchlorate brines are above $\sim 10^{-5}$ mol m⁻³ and vary across the surface by 1-2 orders of magnitude (see Figure 2d).

We extended our results to examine how O₂ solubility in Ca- and Mg-perchlorate brines varies with climates at different obliquities. For BE and WC with supercooling, we observed that the range and average of O₂ solubility significantly decreased for higher obliquities, due to an increase of the minimum values and a decrease of the maximum values for the annually averaged surface temperature across the planet's surface. Integrating these results with obliquity variation through time²², we found that the past 5

Ma have supported particularly O₂-rich environments (Figure 3b), while the preceding 15 Ma supported average maximum O₂ solubility values ~200 times lower than today. These results demonstrate substantial secular variation in the potential O₂ content of fluids in Mars surface environments over recent geological time.

We found that on modern-day Mars—including all uncertainties, for our best estimate and worst case, with and without supercooling—the solubility of O₂ in various fluids exceeds by at least 1-2 orders of magnitude the level required for aerobic respiration²¹ by microbes (see Figure 1e and 2). Thus, Mars could offer a wide range of surface and near-surface environments containing enough dissolved oxygen to support aerobic respiration like that seen in diverse groups of terrestrial microorganisms. Moreover, for supercooled Ca- and Mg-perchlorate brines on Mars today, ~6.5% of the surface at latitudes above 70° (north and south) could support dissolved O₂ concentrations far higher—levels sufficient to sustain respiration demands of complex multicellular organisms (Figure 1d). Such aerobic oases with $[O_2]_{aq} > 2 \cdot 10^{-3} \text{ mol m}^{-3}$ are feasible for low obliquities and become unlikely for obliquities above ~50° (Figure 3a) (such high-obliquity states did not happen in the last 20 Ma, but might have existed in the deeper Martian past²³). Other aerobic environments with $[O_2]_{aq} \sim 10^{-4} - 10^{-3} \text{ mol m}^{-3}$ can occur closer to the equator in higher pressure regions like Hellas, Arabia Terra, Amazonis Planitia, and Tempe Terra (Figure 2).

At the levels for molecular oxygen solubility that we find, O₂ would be expected to play a role in chemical weathering of Mars' crust³⁰—potentially explaining a range of geochemical and geologic data, such as highly oxidized phases in Martian rocks^{18,19}.

We do not know whether Mars was ever a host to life. On Earth, aerobic respiration appears to have followed in the evolutionary footsteps of oxygenic photosynthesis. However, Mars shows us this need not be the case, broadening our view of the opportunities for aerobes on other planetary bodies.

1 Figures for main text

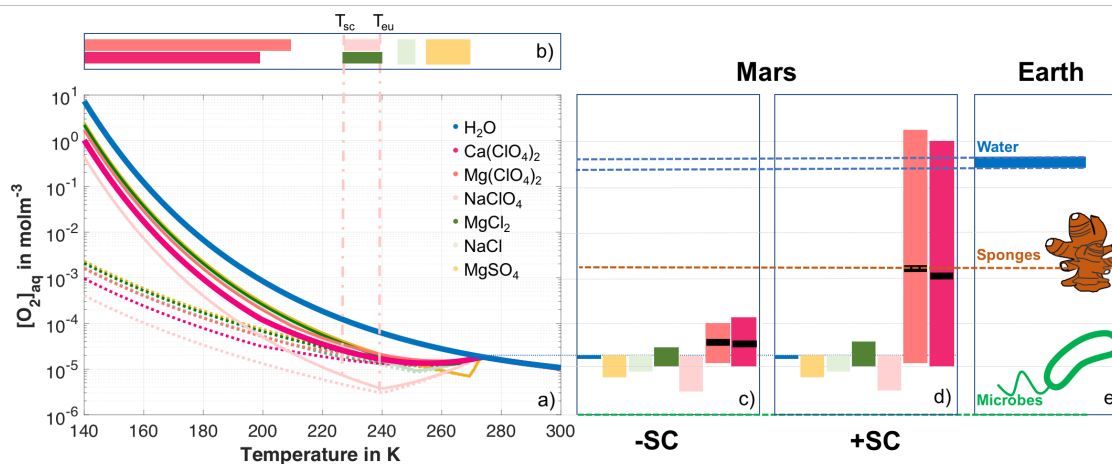


Figure 1 – Solubility of O_2 , $[O_2]_{aq}$, in liquid water and brines on Mars. a) $[O_2]_{aq}$ change with temperature at a pressure of 6.1 mbar using the minimum salt concentration that keeps the brine liquid^{7,8,25} (best estimate, BE, is *solid*, worst case, WC, is *dashed*). b) Supercooling feasible between eutectic temperature, T_{eu} , and T_{sc} ^{7,8,25}. c, d) Bars represent BE $[O_2]_{aq}$ range with (+SC) and without supercooling (-SC). *Solid black* line shows upper $[O_2]_{aq}$ limit reduction (if any) for WC. e) Blue bar shows the $[O_2]_{aq}$ range for water with $T \sim 273\text{--}300$ K and 1 bar, dashed lines show the O_2 levels required for aerobic respiration by microbes²¹ (green) and animals⁹ (orange).

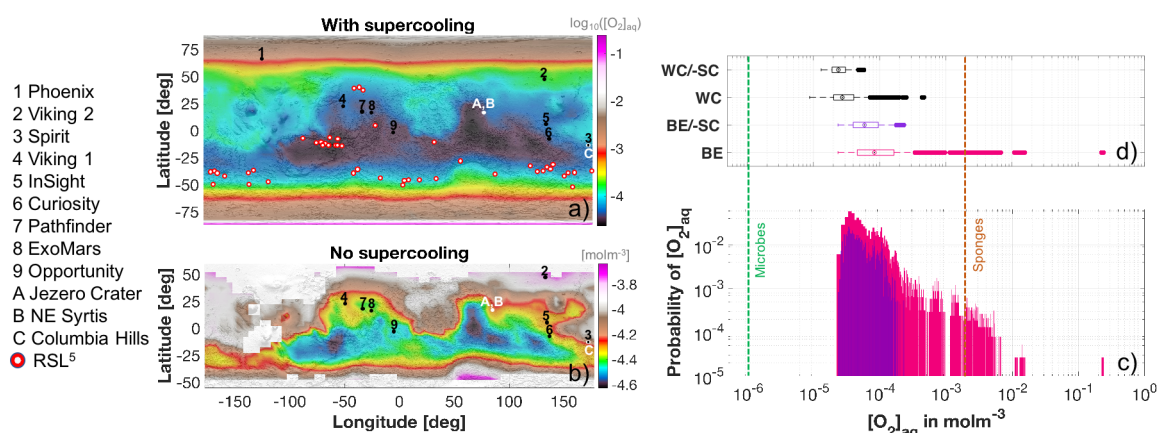


Figure 2 – Climatically-induced spatial variation of O_2 solubility in Ca-perchlorate brines on modern-day Mars: a, b) Maps of $[O_2]_{aq}$ according to the best estimate (BE) for the annually averaged O_2 solubility $[O_2]_{aq}$ in Ca-perchlorate brines with (a) and without (b) supercooling under modern Martian conditions with a perennial south polar CO_2 cap. Without supercooling, only latitudes within $\sim 50^\circ$ favor liquid brines. **c)** Histogram of $[O_2]_{aq}$ values for BE with (red) and without (purple) supercooling and biological breathing limits. **d)** Boxplots of BE and worst case (WC) with supercooling and without ($/-SC$). $[O_2]_{aq}$ exceeds the lower limit for aerobic respiration by microbes, and in certain environments, surpasses the $[O_2]_{aq}$ limit for sponges. Results very similar for Mg-perchlorate.

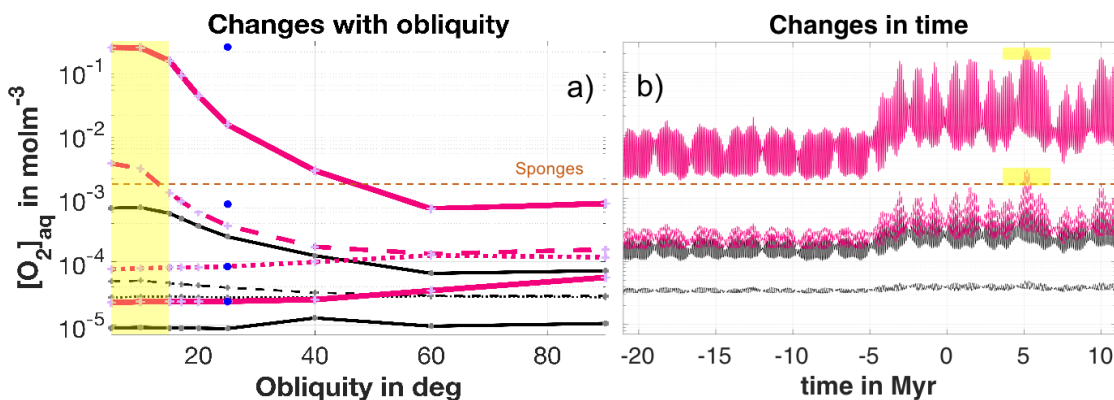


Figure 3 – Obliquity-driven evolution of aerobic environments on Mars across time:

a) With supercooling, best estimate (BE, purple crosses with red line) and worst case (WC, gray crosses with black line) for global maximum (top solid), minimum (bottom solid), average (dashed), and median (dotted) O_2 solubilities in Ca-perchlorate brines with varying obliquity without a perennial south polar cap (SPC) (blue dots are BE results with SPC, see Figure 2). **b)** Calculations of how $[O_2]_{aq}$ varies during past and future obliquity changes²³ showing the global maximum (top) and average (bottom) $[O_2]_{aq}$ values across time. Highlighted in a dashed orange line is the aerobic limit for sponges and obliquities/times where atmospheric collapse occurs (yellow).

References

- 1 Catling, D. C., Glein, C. R., Zahnle, K. J. & McKay, C. P. Why O₂ Is Required by Complex Life on Habitable Planets and the Concept of Planetary “Oxygenation Time”. *Astrobiology* **5**, 415-438 (2005).
- 2 Fischer, W. W., Hemp, J. & Johnson, J. E. Evolution of Oxygenic Photosynthesis. *Annu. Rev. Earth Planet. Sci.* **44**, 647–683, doi:10.1146/annurev-earth-060313-054810 (2016).
- 3 Nair, H., Allen, M., Anbar, A. D., Yung, Y. L. & Clancy, R. T. A Photochemical Model of the Martian Atmosphere. *Icarus* **111**, 124-150, doi:10.1006/icar.1994.1137 (1994).
- 4 Ojha, L., et al. Spectral evidence for hydrated salts in recurring slope lineae on Mars. *Nature Geoscience* **8**, 829-832, doi:10.1038/ngeo2546 (2015).
- 5 Rummel, J. D. *et al.* A new analysis of Mars "Special Regions": findings of the second MEPAG Special Regions Science Analysis Group (SR-SAG2). *Astrobiology* **14**, 887-968, doi:10.1089/ast.2014.1227 (2014).
- 6 Kounaves, S. P. *et al.* Identification of the perchlorate parent salts at the Phoenix Mars landing site and possible implications. *Icarus* **232**, 226–231, doi:10.1016/j.icarus.2014.01.016 (2014).
- 7 Toner, J. D., Catling, D. C. & Light, B. The formation of supercooled brines, viscous liquids, and low-temperature perchlorate glasses in aqueous solutions relevant to Mars. *Icarus* **233**, 36-47, doi:10.1016/j.icarus.2014.01.018 (2014).

- 8 Pestova, O. N., Myund, L. A., Khripun, M. K. & Prigaro, A. V. Polythermal Study of the Systems $M(\text{ClO}_4)_2\text{-H}_2\text{O}$ ($M^{2+} = \text{Mg}^{2+}, \text{Ca}^{2+}, \text{Sr}^{2+}, \text{Ba}^{2+}$). *Russian Journal of Applied Chemistry* **78**, 409-413 (2005).
- 9 Mills, D. B. *et al.* Oxygen requirements of the earliest animals. *Proc Natl Acad Sci U S A* **111**, 4168-4172, doi:10.1073/pnas.1400547111 (2014).
- 10 Grotzinger, J. P. & Milliken, R. E. The sedimentary record of Mars: distribution, origins, and global stratigraphy. *Sedimentary Geology of Mars*, SEPM Special Publication, 1-48 (2012).
- 11 François, L. M., Walker, J. C. G. & Kuhn, W. R. A numerical simulation of climate changes during the obliquity cycle on Mars. *Journal of Geophysical Research* **95**, 14761, doi:10.1029/JB095iB09p14761 (1990).
- 12 Jakosky, B. M. *et al.* Mars' atmospheric history derived from upper-atmosphere measurements of $^{38}\text{Ar}/^{36}\text{Ar}$. *Science* **355**, 1408–1410 (2017).
- 13 Grotzinger, J. P. *et al.* Deposition, exhumation, and paleoclimate of an ancient lake deposit, Gale crater, Mars. *Science* **350**, aac7575, doi:10.1126/science.aac7575 (2015).
- 14 Leshin, L. A. *et al.* Volatile, isotope, and organic analysis of martian fines with the Mars Curiosity rover. *Science* **341**, 1238937, doi:10.1126/science.1238937 (2013).
- 15 Marion, G. M., Catling, D. C., Zahnle, K. J. & Claire, M. W. Modeling aqueous perchlorate chemistries with applications to Mars. *Icarus* **207**, 675-685, doi:10.1016/j.icarus.2009.12.003 (2010).

- 16 Mahaffy, P. R. *et al.* Abundance and isotopic composition of gases in the martian atmosphere from the Curiosity rover. *Science* **341**, 263-266, doi:10.1126/science.1237966 (2013).
- 17 Shaheen, R., Niles, P. B., Chong, K., Corrigan, C. M. & Thiemens, M. H. Carbonate formation events in ALH 84001 trace the evolution of the Martian atmosphere. *Proc Natl Acad Sci U S A* **112**, 336-341, doi:10.1073/pnas.1315615112 (2015).
- 18 Lanza, N. L., et al. . High manganese concentrations in rocks at Gale crater, Mars. *Geophys. Res. Lett.* **41**, 5755–5763, doi:10.1002/2014GL060329 (2014).
- 19 Lanza, N. L., et al. . Oxidation of manganese in an ancient aquifer, Kimberley formation, Gale crater, Mars. *Geophys. Res. Lett.* **43**, 7398–7407, doi:10.1002/2016GL069109 (2016).
- 20 Arvidson, R. E. *et al.* High concentrations of manganese and sulfur in deposits on Murray Ridge, Endeavour Crater, Mars. *American Mineralogist* **101**, 1389–1405, doi:10.2138/am-2016-5599 (2016).
- 21 Zakem, E. J. & Follows, M. J. A theoretical basis for a nanomolar critical oxygen concentration. *Limnology and Oceanography* **62**, 795-805, doi:10.1002/lno.10461 (2017).
- 22 Mischna, M. A., Baker, V., Milliken, R., Richardson, M. & Lee, C. Effects of obliquity and water vapor/trace gas greenhouses in the early martian climate. *Journal of Geophysical Research: Planets* **118**, 560–576, doi:10.1002/jgre.20054 (2013).

- 23 Laskar, J. *et al.* Long term evolution and chaotic diffusion of the insolation quantities of Mars. *Icarus* **170**, 343-364, doi:10.1016/j.icarus.2004.04.005 (2004).
- 24 Archer, D. G. & Carter, R. W. Thermodynamic Properties of the NaCl + H₂O System. 4. Heat Capacities of H₂O and NaCl(aq) in Cold-Stable and Supercooled States. *J. Phys. Chem. B* **104**, 8563-8584 (2000).
- 25 Toner, J. D. & Catling, D. C. Water activities of NaClO₄, Ca(ClO₄)₂, and Mg(ClO₄)₂ brines from experimental heat capacities: Water activity >0.6 below 200K. *Geochimica et Cosmochimica Acta* **181**, 164-174, doi:10.1016/j.gca.2016.03.005 (2016).
- 26 Clegg, S. L. & Brimblecombe, P. The solubility and activity coefficient of oxygen in salt solutions and brines. *Geochimica et Cosmochimica Acta* **54**, 3315-3328 (1990).
- 27 Konnik, E. I. Salting-out and Salting-in of Gaseous Non-electrolytes in Aqueous Solutions of Electrolytes. *Russian Chemical reviews* **46**, 577-588 (1977).
- 28 Pitzer, K. S. Theoretical considerations of solubility with emphasis on mixed aqueous electrolytes. *Pure & Appl. Chem.* **58**, 1599-1610 (1989).
- 29 Tromans, D. Modeling Oxygen Solubility in Water and Electrolyte Solutions. *Ind. Eng. Chem. Res.* **39**, 805-812 (2000).
- 30 Johnson, J. E., Gerpheide, A., Lamb, M. P. & Fischer, W. W. O₂ constraints from Paleoproterozoic detrital pyrite and uraninite. *Geological Society of America Bulletin*, doi:10.1130/B30949.1 (2014).

2 Methods

Below we summarized all methods—from solubility to global circulation model—needed to reproduce our results. We direct the reader to our Supplementary Online Material (SOM) for details on any of the methods subsections.

Solubility model. The solubility of O₂ is the number of dissolved O₂ molecules ($[\widetilde{O}_2]_{aq,X}$ in mol kg⁻¹ and $[O_2]_{aq,X}$ in mol m⁻³) in a brine consisting of m_X mol of salt X per kg of pure water in equilibrium with an atmosphere of pressure, P , partial O₂ volume fraction, f_{O_2} ($f_{O_2}P$ corresponds to the total partial O₂ pressure in the atmosphere), and surface temperature, T .

To compute the solubility, $[\widetilde{O}_2]_{aq,X}$, we started with the solubility of O₂ in pure water, $[\widetilde{O}_2]_{aq,w}$.

$$[\widetilde{O}_2]_{aq,w}(T, P) = \frac{f_{O_2}P}{P_{ref}} \exp\left(\frac{\tilde{\mu}_{g,O_2}(T) - \tilde{\mu}_{aq,w,O_2}(T)}{RT}\right) \quad (1)$$

$\tilde{\mu}(T)$ is the chemical potential as a function of temperature at fixed reference pressure P_{ref} – with $\tilde{\mu}_{g,O_2}(T)$ for O₂ in the gas phase and $\tilde{\mu}_{aq,w,O_2}(T)$ for O₂ dissolved in water.

To compute the solubility of O₂ in pure water, $[\widetilde{O}_2]_{aq,w}$, we needed to determine the difference in molar chemical potential evaluated at the reference pressure P_{ref} between O₂ dissolved in pure water and in the gas phase $\Delta\tilde{G}(T) = \tilde{\mu}_{aq,w,O_2}(T) - \tilde{\mu}_{g,O_2}(T)$ as a function of temperature, in J mol⁻¹. The difference in chemical potential corresponds to the difference in molar Gibbs potential between O₂ in the gaseous and dissolved phases.

$$\tilde{\mu}(T) = \tilde{\mu}(T_{ref}) - S(T_{ref})[T - T_{ref}] + \int_{T_{ref}}^T C_P(T')dT' - T \int_{T_{ref}}^T \frac{C_P(T')}{T'}dT' \quad (2)$$

To calculate the chemical potential as a function of temperature at fixed reference pressure, $\tilde{\mu}(T)$, either for O₂ in the gas phase or in the dissolved phase, we needed to know the values of their chemical potentials $\tilde{\mu}(T_{ref})$ and molar entropy $S(T_{ref})$, in J K⁻¹ mol⁻¹, at a reference temperature, T_{ref} —both were previously measured in experiments³¹—and the temperature dependence of the molar specific heat at constant pressure, $C_P(T)$, in J K⁻¹ mol⁻¹. The parameters needed to solve Equations 1-2 are listed in Table S1 and can be found in the literature³¹. For the choice of the temperature dependence of the specific heat capacity at constant pressure of gaseous and dissolved O₂ see the Section below on “*Specific heats and robustness of conclusions*”.

After having computed the solubility of O₂ in pure supercooled water, we needed to quantify the electrostatic interactions between the water dipoles and the ions in solution because this causes a reduction in apparent water volume that can be used to dissolve O₂^{29,31,32}, and hence the solubility of O₂ in a brine containing a salt, X, of molality m_X is reduced by a salting out factor of $\gamma_{O_2}(X, m_X)$ compared to pure water.

$$[\widetilde{O}_2]_{aq,X}(T, P) = \frac{1}{\gamma_{O_2}(X, m_X)} [\widetilde{O}_2]_{aq,w}(T, P) \quad (3)$$

Experiments demonstrated that the salting out factor $\gamma_{O_2}(X, m_X)$ depends only weakly on temperature^{26,33}, and thus the temperature dependence is usually neglected^{33,34}. In the SOM, we added all the available data on various salts from 300-240 K as well as theoretical calculations, which indicate that too for perchlorates, we expect from 298-140 K

only a weak temperature-induced increase of $\gamma_{O_2}(X, m_X)$ by less than a factor of 3-10 (and likely less than 5).

The electrostatic interactions can be separated into first-order direct undisturbed interactions between the O_2 molecules and the dissolved cations, (O_2 -c), and anions, (O_2 -a), respectively. Such interactions are described with the Pitzer approach²⁸ through interaction coefficients λ_{O_2-c} and λ_{O_2-a} and the corresponding molalities for the cations m_c and anions m_a respectively. The secondary interaction between the triplet of cations, anions, and O_2 molecules λ_{O_2-c-a} is negative^{26,28} because secondary interactions generally weaken the electrostatic primary exchange of cations or anions with the O_2 molecule, which therefore decreases the salting out factor, and leads to an effective increase of the gas solubility. Setting $\lambda_{O_2-c-a} = 0$ marks hence a lower bound for the solubility. To make the salting out factor a function of salt molality, m_X , we used for each ion (cation and anion) the mol(ion)/mol(salt) fractions, f_c and f_a . The parameters needed to solve Equations 3-4 can be found in Table S2, and can be taken or computed with available data^{26,27,35}.

$$\begin{aligned} \gamma_{O_2}(X) &= \exp\left(\sum_c 2\lambda_{O_2-c}m_c + \sum_a 2\lambda_{O_2-a}m_a + \sum_c \sum_a \lambda_{O_2-c-a}m_c m_a\right) \\ &= \exp\left(2\sum_c \lambda_{O_2-c}f_c m_X + 2\sum_a \lambda_{O_2-a}f_a m_X + \sum_a \sum_c \lambda_{O_2-c-a}f_a f_c m_X^2\right) \quad (4) \end{aligned}$$

We converted the solubility of O_2 from mol kg⁻¹ $[\widetilde{O}_2]_{aq,X}$ into mol m⁻³ $[O_2]_{aq,X}$ (which is shown in Figures 1-3) because it is the volume number density that is relevant to chemistry and respiration.

$$[O_2]_{aq,X}(T, P) = \rho_{brine}(T, P) \cdot [\widetilde{O}_2]_{aq,X}(T, P) \quad (5)$$

The density of brines is only slightly temperature-dependent, can be well approximated by an incompressible fluid, and increases with decreasing temperatures by less than 5-10% from 298-140 K (see SOM). Therefore, by making the assumption that $\rho_{brine}(T, P) \approx \rho_w(T_{ref}, P_{ref}) \approx 1000 \text{ kg m}^{-3}$, we attained a lower estimate for the solubility of O_2 .

Together, Equations 1-5 allowed us to calculate the solubility of O_2 in a variety of brines, across a wide range of temperatures, including those far below the freezing point of pure water, with the specific heat of dissolved O_2 as the major modulating factor.

Specific heats and robustness of conclusions. The specific heat at constant pressure of O_2 in the gas phase is experimentally well known down to 100 K and remains approximately constant³⁶ from 300-100 K with $C_{P,O_2,g}(T) \approx 29.332 \text{ J K}^{-1} \text{ mol}^{-1}$ due to translational and rotational degrees of freedom remaining active throughout this temperature range.

The major factor impacting the solubility of O_2 in pure water is the heat capacity of dissolved O_2 as a function of temperature $C_{P,O_2,aq}(T)$. Larger values of $C_{P,O_2,aq}(T)$ lead to a greater gas solubility. For temperatures between 273-373 K, experiments showed that $C_{P,O_2,aq}(T)$ increases linearly with decreasing temperature towards 273 K, there is no data below 273 K for $C_{P,O_2,aq}(T)$. As we demonstrated in the SOM, there is good evidence that a trend of increasing heat capacity persists until at least ~ 225 -235 K, where water might have a liquid-liquid phase transition²⁴, possibly leading to a decay of the specific heat of dissolved O_2 for smaller temperatures.

Because of this uncertainty, we took a more conservative approach by considering 1) a best estimate (BE) with $C_{P,O_2,aq}(T) = C_{P,O_2,aq}(T = 298\text{ K})$; 2) reasonable alternatives for the specific heat capacity as a function of temperature either based on the specific heat for supercooled water or a linear decay towards 140 K (similar to the specific heat of various brines^{24,25}) — leading to results of only less than a factor of ~ 3 smaller at 140 K than what we found with BE; demonstrating the robustness of our conclusions with BE; and 3) a worst-case limit to the solubility of O_2 in water (WC) (see below, and in much more detail in the Supplementary Online Material), as shown in Figure 1 and Figure S1. WC is technically an unreachable limit that would lead at 140 K to a solubility about three orders of magnitude smaller than found with BE. Although this worst case would limit high- O_2 oases with concentrations above the breathing limit for sponges⁹, it would still permit O_2 solubilities orders of magnitude above the aerobic limit for microorganisms²¹ for Martian conditions.

Thermodynamic limit and worst-case scenario. The specific heat of dissolved O_2 , $C_{P,O_2,aq}$, controls the solubility of O_2 in pure water or brine in the following manner (using Equations 1 and 3; compare with Equations S11 and S13):

$[O_2]_{aq}(T, \zeta) = F(T) \exp\left(\frac{\zeta(T)}{RT}\right)$ with

$$\zeta(T) = - \int_{T_{ref}}^T C_P(T') dT' + T \int_{T_{ref}}^T \frac{C_P(T')}{T'} dT' \quad (6)$$

$F(T)$ is defined as the solubility of O_2 if the specific heat of dissolved O_2 in water were always zero, and is well-constrained and monotonically increases for smaller temperatures.

The function $\zeta(T)$, defined in Equation 6, contains all the uncertainties introduced by the behavior of $C_{P,O_2,aq}(T)$ below 273 K. In the SOM, we demonstrated that the function $\zeta(T)$ must also monotonically increase with decreasing temperatures due to the specific heat being always larger than zero, for $T > 0$ K.

Therefore, we can obtain a thermodynamic limit to the solubility of O_2 in pure water by setting the specific heat of dissolved O_2 for temperatures below 273 K to an unreachable minimum value of zero, and, hence, the minimum solubility of O_2 in pure water $T < 273$ K is given by:

$$[O_2]_{aq}(T, \zeta)|_{min} = [O_2]_{aq}(T, \zeta^*) \text{ with } \zeta^*(T) = \zeta(T = 273 \text{ K}) \quad (7)$$

Melting curve for brines. Values for the critical concentration at temperature, T , needed to keep the brine liquid, $m_X(T)$, were taken from experimental data^{7,25,37} and fit with a third-degree polynomial to generate a melting curve for the brine. Inside the temperature domain where the brine is known to effectively supercool (between T_{eu} and T_{sc} , see Figure 1b) we assumed $m_{eu} = m_X(T_{eu})$, as no additional salt has to be added to keep the brine liquid, where T_{eu} and m_{eu} are the eutectic temperature and the eutectic concentration respectively. Therefore, we obtained $m_X(T) = \sum_{i=0}^3 p_i T^i$ for $T > T_{eu}$ and $m_X(T) = m_{eu} = m_X(T_{eu})$ for $T \leq T_{eu}$. Moreover, the eutectic temperature is not a strong function of pressure, and the pressures on Mars support the liquid state of the Ca-perchlorate brines assumed in Figure 2 (see SOM). For parameters, see Table S3.

Boxplots and statistics. We used the statistical toolbox in MATLAB 2016a. The box

width (shown in Figure 2) represents the inter quartile range, with notch marks at the 95% confidence interval for the median circle. The dashed whiskers indicate 2.698σ . Data beyond 2.7σ are show in dots outside the whiskers.

General circulation model for Mars. We used the Mars Weather Research and Forecasting (MarsWRF) GCM for this investigation. MarsWRF³⁸ is a Mars-specific implementation of the PlanetWRF GCM³⁹—a global model derived from the terrestrial mesoscale WRF model⁴⁰. MarsWRF solves the primitive equations using a finite difference methodology on an Arakawa-C grid⁴¹. Both the horizontal and vertical resolution of the model are variable and selectable at run time; a 40-layer vertical grid (from 0-80 km) was used, following a modified-sigma (terrain-following) coordinate. The lowest model layer is ~75-100 m above ground level, depending on location and season. We used a horizontal resolution of $5^\circ \times 5^\circ$, which corresponded to a grid of 72 points in longitude x 36 points in latitude. The total present-day atmospheric CO₂ budget, as well as the CO₂ ice albedo and emissivity for each hemisphere, were adjusted until the modeled pressure curves best matched those observed at the Viking Lander 1 and 2 sites⁴². Both surface albedo and thermal inertia were matched to MGS-TES observations^{43,44}, while water ice albedo and emissivity were fixed at 0.45 and 1.0, respectively.

The model includes a basic water cycle, which allows the condensation, sublimation, sedimentation, and transport of water ice particles in the atmosphere, and growth and recession of polar water ice caps. Surface albedo was modified to the aforementioned values when either CO₂ or water ice condensed on the surface.

Planetary obliquity, or axial tilt, can be modified at runtime in MarsWRF⁴⁵. In all obliquity simulations, we held other model parameters constant. To examine the past 20 Ma of Mars history, we assumed the luminosity of the Sun to be at the present-day value. Because the frost-point temperature for CO₂ (~148 K at present surface pressure) was regularly reached in the polar winter hemisphere, the present-day Martian atmosphere cycles ~25% of its total mass over the course of the year into and out of the polar caps. For obliquities higher than present-day (~25°), this fraction is somewhat larger. Furthermore, for obliquities below ~15°, solar heating of the polar regions was insufficient to stave off condensation year-round, and Mars experiences episodes of atmospheric collapse, where the condensable species in the atmosphere (predominantly CO₂) formed thick ice caps at the poles. These intervals are indicated in light green in Figure 3, and, if theoretical predictions of obliquity as a function of time are correct, are not seen in the past 20 Ma and will rarely occur in the next 10 Myr²³.

At higher obliquities, water ice preferentially condensed at lower latitudes. While there is disagreement over exactly how widespread such water deposits might be^{45,46}, MarsWRF handles the tropical ice deposits self-consistently, increasing surface albedo at locations where ice is deposited. With all else equal, Mars at high obliquity will have a slightly lower global surface temperature than at present values due to the increased surface area in the tropics covered by high albedo ice, as compared to the relatively small polar area covered by ice at present. However, the maximum (minimum) values of annually averaged surface temperature will generally decrease (increase) with increasing obliquity – mainly due to the albedo changes associated with obliquity change as mentioned before (see SOM for a more

detailed discussion). The distribution, minimum, average, and maximum values of annually averaged surface temperature can be found in Table S4 as well as in Figure S4. These simulations showed that obliquity variation with time was the major driver for differences in annual averages for surface temperature and pressure; past variations in eccentricity played only a minor role in affecting annually averaged surface temperatures and pressures.

To compare different obliquities, we do not account for Mars' south polar residual CO₂ cap (SPC), which would only reduce the annually averaged surface temperatures, and hence increase the solubility of O₂, as shown for a modern-day obliquity of $\sim 25^\circ$ in Figure 3a.

Additional references for methods

- 31 Tromans, D. Temperature and pressure dependent solubility of oxygen in water: a thermodynamic analysis. *Hydrometallurgy* **48**, 327-342 (1998).
- 32 Tromans, D. Oxygen solubility modeling in inorganic solutions: concentration, temperature and pressure effects. *Hydrometallurgy* **50**, 279–296 (1998).
- 33 Silvester, L. F. & Pitzer, K. S. Thermodynamics of electrolytes. X. Enthalpy and the effect of temperature on the activity coefficients. *Journal of Solution Chemistry* **7**, 327–337, doi:10.1007/BF00662893 (1978).
- 34 Toner, J. D., Catling, D. C. & Light, B. A revised Pitzer model for low-temperature soluble salt assemblages at the Phoenix site, Mars. *Geochimica et Cosmochimica Acta* **166**, 327-343, doi:10.1016/j.gca.2015.06.011 (2015).
- 35 Khomutov N. E., K. E. I. Solubility of oxygen in aqueous electrolyte solutions. *Russian Journal of Physical Chemistry* **48** (1974).
- 36 Manion, J. A. *et al.* in *NIST Standard Reference Database 17* Vol. 17, Version 7.0 (Web Version), Release 1.6.8, Data Version 2016.10 (National Institute of Standards and Technology, Gaithersburg, Maryland, 20899-8320, 2016).
- 37 Li, D. *et al.* Phase diagrams and thermochemical modeling of salt lake brine systems.II. NaCl+H₂O, KCl+H₂O, MgCl₂+H₂O and CaCl₂+H₂O systems. *CALPHAD: Computer Coupling of Phase Diagrams and Thermochemistry* **53**, 78-89, doi:10.1016/j.calphad.2016.03.007 (2016).
- 38 Toigo, A. D., Lee, C., Newman, C. E. & Richardson, M. I. The impact of resolution on the dynamics of the martian global atmosphere: Varying resolution

- studies with the MarsWRF GCM. *Icarus* **221**, 276-288, doi:10.1016/j.icarus.2012.07.020 (2012).
- 39 Richardson, M. I., Toigo, A. D. & Newman, C. E. PlanetWRF: A general purpose, local to global numerical model for planetary atmospheric and climate dynamics. *Journal of Geophysical Research* **112**, doi:10.1029/2006je002825 (2007).
- 40 Skamarock, W. C. & Klemp, J. B. A time-split nonhydrostatic atmospheric model for weather research and forecasting applications. *Journal of Computational Physics* **227**, 3465-3485, doi:10.1016/j.jcp.2007.01.037 (2008).
- 41 Arakawa, A. & Lamb, V. R. Computational design of the basic dynamical processes of the UCLA general circulation model. *Methods Comput. Phys.* **17**, 173-265 (1977).
- 42 Guo, X., Lawson, W. G., Richardson, M. I. & Toigo, A. Fitting the Viking lander surface pressure cycle with a Mars General Circulation Model. *Journal of Geophysical Research* **114**, doi:10.1029/2008je003302 (2009).
- 43 Christensen, P. R. *et al.* Mars Global Surveyor Thermal Emission Spectrometer experiment: Investigation description and surface science results. *Journal of Geophysical Research* **106**, 23823-23871 (2001).
- 44 Putzig, N. & Mellon, M. Apparent thermal inertia and the surface heterogeneity of Mars. *Icarus* **191**, 68-94, doi:10.1016/j.icarus.2007.05.013 (2007).

- 45 Mischna, M. A. On the orbital forcing of Martian water and CO₂ cycles: A general circulation model study with simplified volatile schemes. *Journal of Geophysical Research* **108**, doi:10.1029/2003je002051 (2003).
- 46 Forget, F., Haberle, R. M., Montmessin, F., Levrard, B. & Head, J. W. Formation of Glaciers on Mars by Atmospheric Precipitation at High Obliquity. *Science* **311**, 368-371 (2006).

SOM - Supplementary Online Material

In this supplementary section, we derived all equations used in the main article and gave an extended discussion of our methods. It is organized as follows. First, we derived all needed equations in Section 1. In Section 2, we discussed our solubility (2.1) and climate (2.2) models. In Section 3, we explained why the averaging method we employed for computing O₂ solubilities as a function of the annually averaged local values for surface temperature and pressure is practical and underestimates O₂ solubilities and the difference between minimum and maximum values. In Section 4, we elaborate on how pressure and temperature control solubility, and possibly oxidation, gradients across the Martian surface.

1. Detailed derivation of all necessary equations

To compute the solubility of O₂ in pure water $[\widetilde{O}_2]_{aq,w}(T,P)$ in mol kg⁻¹ we started with the equilibrium constant for a given pressure and temperature $k(T,P)$, which is defined for an activity coefficient of dissolved O₂, α , and the fugacity coefficient, γ , of O₂ in the gas phase¹⁻⁴ with f_{O_2} being the volume fraction of O₂ in the atmosphere (for Mars, $f_{O_2} =$

0.00146⁵).

$$k(T, P) = \frac{\alpha[\widetilde{O}_2]_{aq,w}(T, P)}{\gamma f_{O_2}} \quad (S1)$$

Both activity coefficient of dissolved O₂ as well as the fugacity of O₂ in the gas phase are close to one because of the small concentrations of dissolved O₂ and the small pressures that are relevant to our study (independent of temperature, for $[\widetilde{O}_2]_{aq,w} \rightarrow 0$ and $P \rightarrow 0$, the definitions for activity coefficient and fugacity demand that $\alpha \rightarrow 1$ and $\gamma \rightarrow 0$ respectively¹). Therefore, Equation S1 simplifies to:

$$k(T, P) = \frac{[\widetilde{O}_2]_{aq,w}(T, P)}{f_{O_2}} \quad (S2)$$

To compute the solubility $[\widetilde{O}_2]_{aq,w}(T, P)$, we needed to compute the equilibrium constant $k(T, P)$, which is defined by the change in molar Gibbs potential $\Delta G^*(T, P)$ between the dissolved and the gaseous phases¹⁻⁴. $R = 8.3144598 \text{ Jmol}^{-1}\text{K}^{-1}$ is the universal gas constant.

$$k(T, P) = \exp\left(\frac{-\Delta G^*(T, P)}{RT}\right) \quad (S3)$$

The molar Gibbs potential is computed through the chemical potential $\mu(T, P)$ for both the dissolved (μ_{aq,w,O_2}) and gaseous (μ_{g,O_2}) O₂ phases.

$$G^*(T, P) = \left(\frac{\partial G}{\partial N}\right)_{T,P} = \mu(T, P) \quad (S4)$$

And hence $\Delta G^*(T, P) = \mu_{aq,w,O_2}(T, P) - \mu_{g,O_2}(T, P)$. Note that the chemical potential is a function of both temperature, T , and pressure, P . Hence, in order to compute the solubility of O₂ in water, we needed to know the chemical potential of O₂ in the gaseous and

dissolved aqueous phases as a function of temperature and pressure.

We referred to Equation S3, where the chemical potential is defined through the molar Gibbs potential, and to Equation S4 in order to compute $\mu(T, P)$ in relation to a reference state $\mu(T_{ref}, P_{ref})$ - by calculating the differential $d\mu(T, P)$ from (T_{ref}, P_{ref}) to (T, P) using the entropy S , the internal energy U , and the molar volume V for both phases.

$$d\mu(T, P) = dG^*(T, P) = d(U + PV - TS) = dU + VdP + PdV - TdS - SdT \quad (S5)$$

With the definition of the internal heat:

$$dU \equiv \delta Q - PdV \quad (S6)$$

and the definition for the entropy:

$$dS \equiv \frac{\delta Q}{T} \quad (S7)$$

we obtain:

$$d\mu(T, P) = \delta Q - PdV + VdP + PdV - TdS - SdT = VdP - SdT \quad (S8)$$

Therefore, we can rewrite the chemical potential as:

$$\mu(T, P) = \mu(T_{ref}, P_{ref}) + \int_{P_{ref}}^P VdP' - \int_{T_{ref}}^T S(T')dT' \quad (S9)$$

The entropy S is a function of temperature and can be related to the specific heat at constant pressure $C_p(T)$, which is more useful (experimentally directly measurable) than the entropy itself, with Equation S7 and $\delta Q|_P = C_p dT$:

$$S(T) = S(T_{ref}) + \int_{T_{ref}}^T dS$$

$$\begin{aligned}
&= S(T_{ref}) + \int_{T_{ref}}^T \frac{C_P(T')}{T'} dT' + \overbrace{C_P(T) - C_P(T)}^{=0} \\
&= S(T_{ref}) - C_P(T) + \frac{\partial}{\partial T} \left(\overbrace{T \int_{T_{ref}}^T \frac{C_P(T')}{T'} dT'}^{\int_{T_{ref}}^T \frac{C_P(T')}{T'} dT' + C_P(T)} \right) \tag{S10}
\end{aligned}$$

Therefore, we replaced in Equation S9 the integral over the entropy and obtained in Equation S11 the chemical potential at temperature T and reference pressure P_{ref} , which corresponds to the temperature-dependent function in Equation 2 from our Methods Section:

$$\tilde{\mu}(T) = \mu(T, P_{ref}) \tag{S11}$$

$$= \tilde{\mu}(T_{ref}) - S(T_{ref})[T - T_{ref}] + \int_{T_{ref}}^T C_P(T') dT' - T \int_{T_{ref}}^T \frac{C_P(T')}{T'} dT'$$

To fully solve for the chemical potential, we needed to take into account effects by pressure, described by $\int_{P_{ref}}^P V dP'$ in Equation S9: for the gas phase (hence for $\mu_{g,O_2}(T, P)$), we assumed an ideal gas with $PV = RT$ (for one mol) and hence:

$$\int_{P_{ref}}^P V dP' \Big|_g = RT \ln \left(\frac{P}{P_{ref}} \right) \tag{S12}$$

For the dissolved phase, we assumed that the molar volume of dissolved O_2 , V_{aq,O_2} , is smaller than that of water, V_w , and hence we get $V_{aq,O_2} = \lambda V_w$ with $0 < \lambda < 1$. Using this volume estimate with the standard molar volume for water at reference temperature and pressure (water is approximately incompressible for the pressures and temperatures that we

are interested in) of $V_w(T_{ref}, P_{ref}) = 18 \cdot 10^{-6} m^3 mol^{-1}$, we found that $\int_{P_{ref}}^P V_{aq, O_2} dP'$ is negligible and would, if included, only increase the solubility of O_2 by about 0.1%.

Therefore, from relationships S9, S11, and S12, we obtained Equation S13:

$$[\widetilde{O}_2]_{aq,w}(T, P) = \frac{f_{O_2} P}{P_{ref}} \exp\left(\frac{\tilde{\mu}_{g, O_2}(T) - \tilde{\mu}_{aq,w, O_2}(T)}{RT}\right) \quad (S13)$$

which corresponds to Equation 1 in our Methods Section (compare also with other sources^{1,3,4}). Note that the here derived pressure dependence corresponds to Henry's law.

From here, to compute $\tilde{\mu}_{g, O_2}(T) - \tilde{\mu}_{aq,w, O_2}(T)$, we needed standard values at (T_{ref}, P_{ref}) for the chemical potentials and entropy of gaseous and dissolved O_2 and the specific heat of O_2 in the gas phase, $C_{P, O_2, g}(T)$, and dissolved in pure water, $C_{P, O_2, aq}(T)$, as a function of temperature. Experiments⁶ confirmed that $C_{P, O_2, g}(T) = C_{P, O_2, g}(T_{ref})$; all parameters at reference conditions can be found in Table 1S.

We examined the choice for the specific heat of dissolved O_2 in pure water in more detail below in the next Section 2.1 and the effects of salts on the solubility of O_2 in Sections 2.1.3 and 2.1.4.

2. Extended Discussion

2.1. Solubility

2.1.1. Specific heat of dissolved O_2 and solubility: tests and robustness of results

Experiments have shown $C_{P, O_2, aq}(T)$ to increase slightly as temperature decreases from 373-273 K, with no data available below this temperature range. There is reason to expect that the trend of increasing heat capacity continues from 273 K to ~225-235 K but possibly

also below this limit. Such a steep increase of $C_{P,O_2,aq}(T)$ is justified by arguing that the behavior of the specific heat of water at cooler temperatures below ~ 300 K directly corresponds to the behavior of the specific heat capacity of dissolved O_2 . This assumption can be partially rationalized, as the smooth increase in the specific heat of pure water from 300 K into the supercooled water domain down to ~ 225 -235 K can be explained by stronger hydrogen bonds at lower temperature¹, and hence a greater amount of heat being needed in order to increase the ambient temperature. This increase in hydrogen bonding for lower temperatures is expected to similarly affect the dissolved O_2 , which will be partially polarized due to the water dipoles, leading potentially to a similar behavior of the specific heats of water and dissolved O_2 below 273 K. However, thermodynamics demands that $\lim_{T \rightarrow 0 K} C_P = 0$. Indeed, some theoretical predictions find that the specific heat of supercooled water could start to decrease again for $T \sim 225$ -235 K, where potentially a liquid-liquid phase transition could occur⁷⁻⁹. We emphasize that experiments to date also allow for the heat capacity to continue increasing into much cooler regions below 235 K.

We used for our nominal best estimate (BE) the simplest assumption that $C_{P,O_2,aq}(T) = C_{P,O_2,aq}(T_{ref})$, but we also tested other reasonable forms of $C_{P,O_2,aq}(T)$ (all show a similar result), and derived a thermodynamic worst case, which technically cannot be reached – assuming the validity of Equations 1 and 2 from our Methods Section.

Assuming $\left(\frac{C_{P,O_2,aq}}{C_{P,w}} \sim const. \right)$ below 273 K (specific heat of dissolved O_2 scales with the specific heat of water) and taking the predicted specific heat behavior⁷⁻⁹ of supercooled water – consisting of an initial power law increase below 273 K towards a critical temperature, T_{crit} , of 225-235 K below which the heat capacity exponentially decays

towards 0 K, we found that at 140 K O₂ solubility values are between 1.2 times smaller or larger than our best estimate (BE). Therefore, if the specific heat of dissolved O₂ behaves similar to the theoretical predictions for the specific heat of supercooled water, then our best estimate is an excellent prediction for the solubility of O₂ below 273 K.

Alternatively, we examined what happens if we had assumed that instead the specific heat of dissolved O₂ in water behaves similar to the specific heat of a “normal fluid” that does not show anomalous behavior like water, such as a very salty NaCl brine⁹. For NaCl-brines⁹ and many other brines including perchlorates¹⁰, the specific heat is rather constant but does decay slowly with decreasing temperature. Assuming an unusually strong linear decrease of $C_{P,O_2,aq}(T)$ by 50% from 293-140 K (a few factors to ~1 order of magnitude larger than generally found for very salty brines^{9,10}), we obtained values for the solubility of O₂ at 140 K that were ~3 times smaller than our best estimate. Thus, we concluded that, for all reasonable forms of $C_{P,O_2,aq}(T)$, the solubility values at 140 K are generally similar to the best estimate assuming a constant heat capacity for dissolved O₂ in pure water. In the next section, we derived a thermodynamic lower bound that cannot be reached.

2.1.2. Specific heat of dissolved O₂ and thermodynamic worst case (WC)

The solubility of O₂ in mol m⁻³ in pure water or brine depends on the specific heat of dissolved O₂, $C_{P,O_2,aq}$, in the following way (see Equations 1 and 3 in Methods Section, and Equations S11 and S13):

$$[O_2]_{aq}(T, \zeta(T)) = F(T) \exp\left(\frac{\zeta(T)}{RT}\right)$$

$$\text{with } \zeta(T) = - \int_{T_{ref}}^T C_P(T') dT' + T \int_{T_{ref}}^T \frac{C_P(T')}{T'} dT' \quad (\text{S14})$$

The function $\zeta(T)$ contains all the uncertainties introduced by the behavior of $C_{P,O_2,aq}(T)$ below 273 K, whereas $F(T)$ depends only on well-constrained properties and monotonically increases for smaller temperatures. We developed a thermodynamic lower limit for $\zeta(T)$, which gives a lower limit for the solubility of O_2 in supercooled water. To achieve this, we needed to assess the behavior of $\zeta(T)$.

First, we showed that $\zeta(T_1) > \zeta(T_2): \forall(T_1 < T_2)$, so independent of the temperature dependence of the heat capacity, solubilities monotonically increase for smaller temperatures, with the minimum solubility curve for $T < 273$ K given by:

$$[O_2]_{aq}(T, \zeta(T)) > [O_2]_{aq}(T) \Big|_{min} = [O_2]_{aq}(T, \zeta^*) \text{ with } \zeta^*(T) = \zeta(T = 273 \text{ K}) \quad (\text{S15})$$

Therefore, the integral in the exponent, which is monotonically increasing for smaller T is cut at the lowermost temperature where $C_{P,O_2,aq}(T)$ is exactly known, at 273 K. Equation S15 was derived in the following: $\forall T: T > 0, C_P(T) > 0$, therefore, because of $T' > T$ and therefore $\frac{T}{T'} < 1$, we have:

$$\left\| T \int_{T_{ref}}^T \frac{C_P(T')}{T'} dT' \right\| < \left\| \int_{T_{ref}}^T C_P(T') dT' \right\| \quad (\text{S16})$$

So, for $T_{ref} > T$, we concluded that:

$$\int_{T_{ref}}^T C_P(T') dT' < 0 \text{ and } \int_{T_{ref}}^T \frac{C_P(T')}{T'} dT' < 0 \quad (\text{S17})$$

$$\text{And hence } \zeta(T) = - \int_{T_{ref}}^T C_P(T') dT' + T \int_{T_{ref}}^T \frac{C_P(T')}{T'} dT' > 0, \forall(T, C_P(T)) \quad (\text{S18})$$

Next to $\zeta(T)$ being a positive function, as shown in Equation S18, $\zeta(T)$ also monotonically increases for smaller T because:

$$\zeta(T_1) = \zeta(T_2) - \overbrace{\int_{T_2}^{T_1} C_P(T') dT'}^{>0 \text{ as shown in S18}} + T \int_{T_2}^{T_1} \frac{C_P(T')}{T'} dT' > \zeta(T_2), \forall (T_1 < T_2) \quad (\text{S19})$$

With Equation S19, we have proven the lower bound for the solubility of oxygen shown in Equation S15. We showed in Figure 1S the worst case in comparison to the best estimate shown in Figure 1 for pure supercooled water.

Note that, formally, the worst case cannot be reached as it demands that $C_P(T) = 0$, and this is only possible for $T = 0 \text{ K}$. Hence, our worst case is indeed an unapproachable limit; however, it provides the logic for a lowermost bound on O_2 solubility, and it is important to note that the true solution is likely to be much greater.

2.1.3. Derivation of Pitzer coefficients for perchlorates

We used the experimental results¹¹⁻¹³ on the O_2 solubility in perchlorate brines containing the salts NaClO_4 , KClO_4 , RbClO_4 , and LiClO_4 to derive the Pitzer interaction coefficients for the O_2 -perchlorate ion interaction $\text{O}_2\text{-ClO}_4^-$, described by $\lambda_{\text{O}_2\text{-ClO}_4^-}$ in Equation 4 in our Methods Section. Generally, the temperature dependence of the Pitzer coefficients is negligible, but we examined this in the next section. The O_2 -cation interaction coefficients, $\lambda_{\text{O}_2\text{-c}}$, for the cations $\text{c}=(\text{Ca}^{2+}, \text{Mg}^{2+})$ were taken from literature¹¹.

We showed the results for the salting out coefficient $\gamma_{\text{O}_2}(X, m_X)$ for a brine containing $m_X \text{ mol kg}^{-1}$ of the salt X in Figure 2S for chlorides and perchlorates (compare with Equation 3 in our Methods Section). There were no direct data on O_2 solubility for Ca- or Mg-perchlorates, and hence there are no data on the secondary Pitzer interaction

coefficients describing the interactions between O_2 -cation- ClO_4^- , λ_{O_2-c-a} . However, as we explained in the Methods Section, the secondary interaction coefficients are generally negative as they represent the disturbance of the respective cation- O_2 and anion- O_2 fields, which drive the solubility of O_2 in the liquid. Hence any reasonable value for $\lambda_{O_2-c-a} < 0$ would only lead to a reduction of the salting out factor $\gamma_{O_2}(X, m_X)$, and would hence result in *greater* solubilities for O_2 in perchlorate brines. Thus, we assume $\lambda_{O_2-c-a} = 0$ for Ca- and Mg-perchlorate brines—and accept that this approach will tend to, if anything, underestimate the solubilities for O_2 in those brines.

2.1.4. Temperature dependence of Pitzer coefficients

It is commonly assumed that the Pitzer coefficients introduced in Equation 4 in the Methods Section are not temperature-dependent^{14,15}. Nonetheless, the wide amount of experimental data that we collected and tested our results against^{11-13,15-19} suggested a slight increase of Pitzer coefficients for smaller temperatures, and thus we labored to find a way to estimate how much this might change the estimate for the O_2 solubilities in Ca- and Mg-perchlorate brines by neglecting a potential temperature dependence of the Pitzer coefficients. We found that the temperature dependence of the Pitzer coefficients could lead to an additional decrease of the solubility of O_2 in Ca- and Mg-perchlorate brines at 140 K by a factor of 3-10 (most likely less than 5).

To derive this estimate, we made use of the salting out theory of Tromans³: he observed that a salt reduced the solubility of O_2 by reducing the molar volume of water (that is dissolving O_2) into an apparent water volume V_{app} . He also found that the change in

apparent water volume could be used to infer the salting out factor. Thus, what we did first was to derive the apparent molar water volume as a function of the brine density ρ_{brine} , molar concentration m_X of the salt X with molecular mass M_X in kg mol^{-1} and molecular crystalline volume V_X , and the molar mass of pure water M_w - leading to Equation S20:

$$V_{app}(T) = \left(\frac{1 + m_X M_X}{\rho_{brine}(T)} - m_X V_X \right) M_w(T) \quad (\text{S20})$$

Equation S20 was easiest to derive by computing the density of the brine ρ_{brine} assuming that water has an apparent volume V_{app} and that the salt preserves its crystalline molecular volume V_X , and solving for V_{app} (for values, see Table 2S).

Second, we computed how this apparent water volume in Equation S20 changes during a reduction of temperature from 298-140 K. The temperature dependence for $V_{app}(T)$ results from the temperature dependence of the brine density and the molar volume of water, but $V_{app}(T)$ is mainly sensitive to small changes in brine density $\rho_{brine}(T)$. Thus, to compute how $V_{app}(T)$ changes with temperature, we focused solely on determining how the density of a brine, $\rho_{brine}(T)$, changes with temperature when salt and molality are fixed.

There is no data or theoretical predictions for the temperature dependence of the density of perchlorate brines, nor is data available on their densities under ambient conditions. To obtain an estimate of how much the density changes for Ca- and Mg-perchlorate brines with up to ~ 4.2 mol of salt per kg water (= 4.2 m, the concentration at the eutectic for Ca-perchlorate^{10,14,20,21}, see Table 3S for values) for a temperature change

from 298-140 K, we turned towards experimental data^{22,23} on the density of a range of brines of different compositions (i.e., NaCl, MgCl₂, CaCl₂, KCl, K₂SO₄, MgSO₄, and Na₂SO₄), and examined how their densities changed from 373-243 K for various salt concentrations up to 30 weight % (or ~4.2 m). We observed that variations in brine density driven by temperature are rather small and would amount to less than a 5-10% increase in density from 298-140 K—assuming a linear increase of the density towards smaller temperatures with a gradient determined between 303-243 K. Note also that our available data indicates that the density variations decrease for smaller temperatures, and one obtains very similar results including data up to 373 K in order to estimate the density gradient with temperature.

The derivation of the density gradient is illustrated in Figure 3S a, where we plotted the density gradient for diverse brines with temperature as a function of molality using density data from 303-243 K. Extrapolating these values would lead to a density increase by less than 5-10% at 140 K in comparison to 298K (on average about 6% for a random sampling of temperature intervals between 303-243 K). Note that this compares excellently with the predicted and measured density variation of NaCl brines between 240-300 K⁹, which would lead to a 5% increase in the NaCl brine density from 298-140 K for a linear extrapolation (which most likely overshoots the density change).

With this approach, we used a density increase of 5-10% for a Ca(ClO₄)₂ brine from 298-140 K to measure the apparent volume changes for a 4.2 m Ca(ClO₄)₂ brine from 298-140 K, $\frac{V_{app}(\varepsilon \cdot \rho_{brine})}{V_{app}(\rho_{brine})} \approx \frac{V_{app}(140 K)}{V_{app}(298 K)}$, where ε is either 1.05 or 1.1 (corresponding to the increase in brine density from 298-140 K by 5-10%). This is illustrated in Figure 3S b,

where we plotted the change in apparent water volume as a function of standard brine density for our 4.2 m $\text{Ca}(\text{ClO}_4)_2$ brine at 298 K. This density was calculated using Equation S20, inverting for the brine density and setting $V_{app}(298\text{ K}) \approx V_w(298\text{ K})$ as a first order approximation. This leads to an estimated 4 m $\text{Ca}(\text{ClO}_4)_2$ brine density at 298 of $\sim 1440\text{ kgm}^{-3}$, and thus values for $\frac{V_{app}(\varepsilon \cdot \rho_{brine})}{V_{app}(\rho_{brine})}$ between 0.875-0.935.

We then used the theory of Tromans³ that can be used to infer how a decrease in apparent volume by a factor of 0.875-0.935 affects the increase in salting out coefficient. Adhering to the reference KOH line of Tromans³ (see his Figure 7 which shows how the salting out factor is a function of apparent volume change), we saw that a temperature change from 298-140 K would maximally yield an increase in salting out factor between ~ 3 -10 (for the average value of 6% density increase from 298-140 K, it would be a factor of ~ 5). Therefore, even if we accounted for a potential temperature dependence of Pitzer coefficients, then we would maximally obtain dissolved O_2 concentrations at 140 K that are 3-10 (and likely less than ~ 5) times smaller than what we observed with our best estimate shown in Figures 1-3.

2.1.5. Stability of perchlorate brines under Martian pressures

For a brine at surface temperature, T, and pressure, P, to be liquid, the concentration of salt must correspond to the critical molality $m_X(T)$ at this temperature (see methods) but the pressure must be also above the triple point pressure $P_{TP}(m_X)$ for that specific brine. For pure water, the triple point pressure is ~ 6.1 mbar, around the average atmospheric pressure on Mars. At this pressure, the melting and boiling temperatures converge, which would

limit the presence for liquid water to temperatures very close to 273 K (this explains the narrow water range in Figure 1c, d).

For brines, however, the triple point pressure is reduced. Specifically, for Ca-perchlorate brines, the salt concentrations m_x needed for the brine to remain liquid at the surface temperatures obtained with our GCM simulations (below ~ 230 K, see Table 4S) result in triple point pressures at least one order of magnitude below the minimal atmospheric surface pressure of ~ 1 mbar encountered in our GCM. The triple point pressure can be approximately computed as the intersection between the standard “water ice-vapor” phase curve in temperature-pressure space and an isotherm for a given temperature $T_{TP} = \max(T, T_{eu})$ (with surface temperatures T ranging from ~ 145 -230 K and the eutectic temperature for Ca-perchlorate brines of $T_{eu} = 198.2$ K). Therefore, the pressure conditions on Mars support the studied Ca-perchlorate brines with salt concentrations $m_x(T)$, which we show in Figure 2, to be liquid. Moreover, due to the approximate incompressibility of water and brines between ~ 1 bar and ~ 1 mbar, we do not expect any significant change in eutectic temperature from Earth to Mars surface pressures.

2.2. Climate model

2.2.1. Albedo variation with obliquity change

The albedo of the Martian surface and how it changes with obliquity can potentially be a significant control on surface temperatures. For any rotating planet, annually averaged insolation at the poles increases going from zero obliquity to larger values, leading to a warming of cooler regions (poles) and a cooling of warmer regions (low latitudes) as

obliquity rises (as seen in Table 4S for annually averaged temperatures for present-day Mars). For a homogenous obliquity across the planet's surface, above 54° obliquity, the poles receive more insolation than the equator,²⁴ and become the 'warmer' regions of the planet on an annual basis, whereas the tropics become the 'cooler' region and, therefore, the preferred location for surface ice formation.

The exact timing of how surface ice on Mars evolves with changing obliquity is uncertain, as is the exact distribution of tropical surface ice at high obliquity. Different studies have alternatively suggested that water ice will condense widely across high topographic and/or high thermal inertia sites on the planet at high obliquity²⁵, or only in localized glacial deposits on the flanks of the Tharsis Montes²⁶. The impact of the exact distribution on surface albedo on temperature can be not insignificant. For example, during the early phases of an obliquity transition (say, from lower to higher values), ice will likely remain in the polar regions for some time after the obliquity rises because of the multi-kilometer thickness of the polar caps. Albedo, then, may remain relatively high at the poles, while it concurrently increases in the tropics due to the development of ice deposits there as obliquity rises. Later in the obliquity transition, though, it is likely that the albedo at the poles will decrease as a darker, dirty sublimation lag forms atop the retreating polar ice cap. The timing of this transition will be gradual and difficult to model precisely.

We performed a series of tests of the end-member cases from previous studies^{25,26}, looking at the effect of their putative ice distributions on the global surface temperatures at high obliquity, looking at different stages of the aforementioned evolution, with bright ice in the poles only, in both the tropics and poles, and in the tropics only. While the annually

averaged global surface temperature does decrease with the presence of tropical ice, (which covers a larger fraction of the surface with high albedo ice than the poles at low obliquity), the general trend in surface temperatures with obliquity continues regardless of the exact distribution of ice, and global mean temperatures continue decreasing with rising obliquity. Differences in surface temperatures between the end members of surface ice distribution are in the range of 5-10 K. This behavior is reflected in the O₂ solubility results in Figure 3a, where, with increasing obliquity, the maximum solubility (corresponding to the lowest annually averaged temperature on the surface) continuously increases.

2.2.2. South pole ice caps

We did not impose any constraints on ice caps for our obliquity calculations; however, on modern-day Mars, observations reveal a perennial polar cap of CO₂ ice in the south, which global climate models cannot self-consistently reproduce without making specific, ad hoc assumptions. In our GCM calculations, we set the surface temperature to the pressure-dependent CO₂ frost point for all locations poleward of -85°. This GCM model is listed in Table 4S as “25° with SPC” and represents the most realistic climate model for modern-day Mars. This model has been used to study modern-day Mars and to create Figure 2 in our main manuscript. Mechanisms for forming such a south polar CO₂ cap are not fully understood, and hence we cannot (and do not) extrapolate it to other obliquities; therefore, we also run a 25° obliquity simulation without the assumption of a south polar cap in order to be able to better grasp how O₂ solubilities change with obliquity, as shown in Figure 3. Note that Figure 3 highlights that the “with SPC” model leads to about one order of

magnitude greater maximum solubility values on the Martian surface today because of the fixed low temperatures for the southern polar regions.

2.2.3. Atmospheric collapse

For obliquities below $\sim 10^\circ$, we found that, on geological timescales, the atmosphere collapses due to the presence of permanent CO₂ cold traps in the polar regions. This can be seen in Table 4S, where we show how the minimum value for the annually averaged surface temperature is pegged to the CO₂ frost point temperature for smaller obliquities. This model scenario is not likely to have occurred in the last twenty million years, might occur rarely in the next five million years (see Figure 3 b), but might have occurred more frequently in the deeper past²⁷.

Atmospheric collapse will, hence, not significantly affect our results, but it is interesting to consider what could happen to O₂ concentrations during such an event. O₂ is produced in the Martian atmosphere through photochemical reactions from CO₂ and H₂O, and subsequent hydrogen escape²⁸; hence, in order to understand how O₂ reacts to atmospheric collapse, we needed to understand how atmospheric water and CO₂ behave during an atmospheric collapse. Atmospheric water will freeze out at the poles due to their lower surface temperatures at smaller obliquities. This will increase O₂ levels²⁹; however, for a reduction of water levels by 1-4 orders of magnitude O₂ levels are only increased by a factor of about three²⁹ – so this effect will be minor. The dominant effect will be the removal of atmospheric CO₂ and, hence, the major source for O₂ formation. It is therefore likely that during an atmospheric collapse O₂ levels will significantly drop.

3. Validity of averaging method and extension to daily temperature variations

For practical reasons, we generated climate data of annual averages of temperature and pressure as a function of location on the Martian surface for varied obliquities (see details on climate model above). The solubility at each point on Mars' surface was evaluated for this annual average of temperature and pressure. It is important to point out that by doing such a time-averaging, the solubility results shown in Figures 1-3 and the differences between minimum and maximum solubilities shown in Figure 3 are smaller than if we instead would have computed the annual average of solubility as a function of hourly or daily averages.

With our averaging approach, we underestimated the solubility because $[O_2]_{aq}$ increases exponentially towards 0 K, hence the gradient $\left| \frac{\partial [O_2]_{aq}}{\partial T} \right|$ is greater for smaller temperatures and the solubility evaluated at the average annual temperature is smaller than the solubility averaged over a greater time (and hence temperature) interval. The solubility is linear in pressure and thus using the annually averaged pressure does represent the precise average for the solubility as a function of pressure. Computing the annual average of the O_2 solubility directly from the non-averaged temperature (daily or hourly) would only increase our O_2 solubility estimates and strengthen the conclusions.

4. Spatial gradients, oxidative weathering, and next steps

As we showed in Figure 4Sa, it is primarily temperature and secondarily pressure that determines the potential solubility of O_2 in Martian surface and near surface environments.

The geographic variations in O₂ content lead to natural gradients in concentrations across environments where waters might naturally flow^{30,31}. Areas where spatial gradients (as shown in Figure 4s b) in O₂ solubility are largest are observed on Tharsis, across Meridiani, Arabia Terra, and within the Hellas basin.

The opportunity for oxidative processes involving O₂ during the chemical weathering of Mars' crust will reflect a convolution between the availability of water and its O₂ content. Our results suggest that we should expect a degree of patchiness in oxidative chemistry associated with weathering; the same would be true for the potential energetic gradients for aerobic respiration.

We have computed the climatically-induced potential for aerobic environments on Mars in 3D (Figure 2), assuming that perchlorate and water are equally available everywhere close to the planet's surface. Naturally, we expect spatial variability in the distribution of water and perchlorates, and hence as a next step, it will be inevitable to explore how perchlorate and water distribution across the Martian surface might vary and how this will affect our results. This, however, demands a much deeper insight into the dynamics of brine formation/destruction and gas dissolution processes, which are far beyond the scope of this first, critical piece of work. It would be also interesting to take into account global Mars Odyssey GRS data on chlorine and hydrogen – however data are only available down to a few microns in depth, are strongly modulated by dust, and cannot see the meaningful depths of the regolith that thermocycle daily or seasonally.

Figures SOM

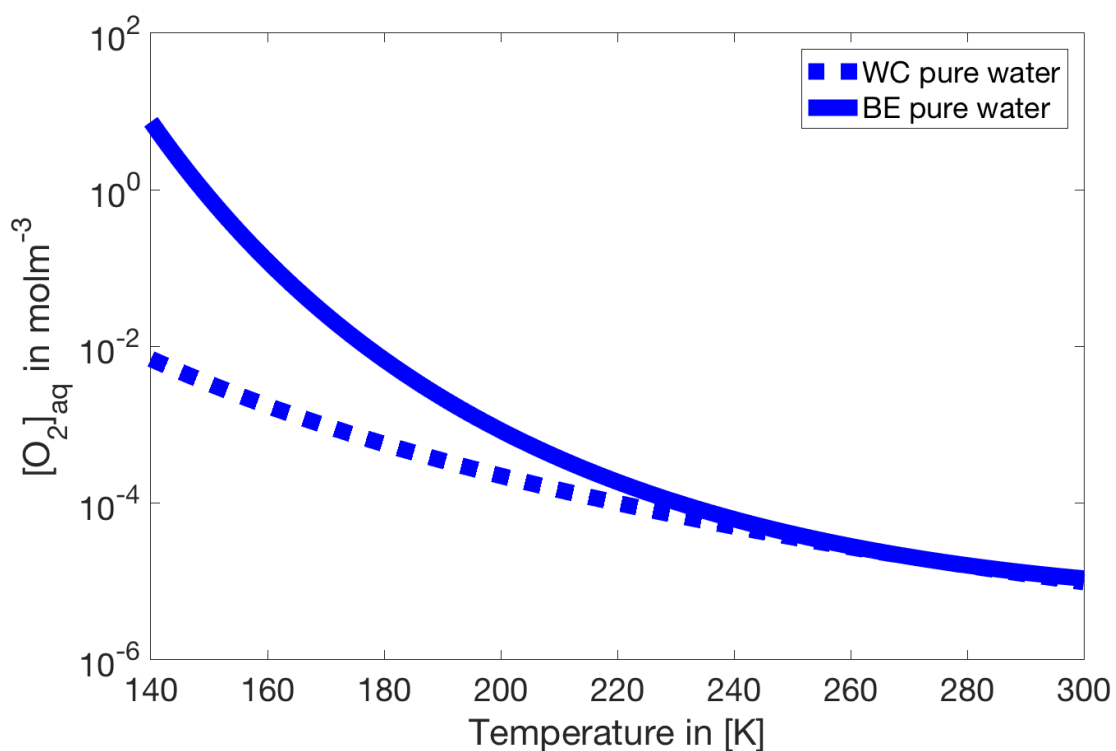


Figure 1S – Thermodynamic lower limit to the solubility of O₂: we compared the best estimate (BE) for the solubility curve of O₂ in supercooled water to the thermodynamic worst case (WC), which sets the specific heat of dissolved O₂ to zero for temperatures below 273 K. Formally, this is only possible for T = 0 K, and thus WC marks a lowermost estimate.

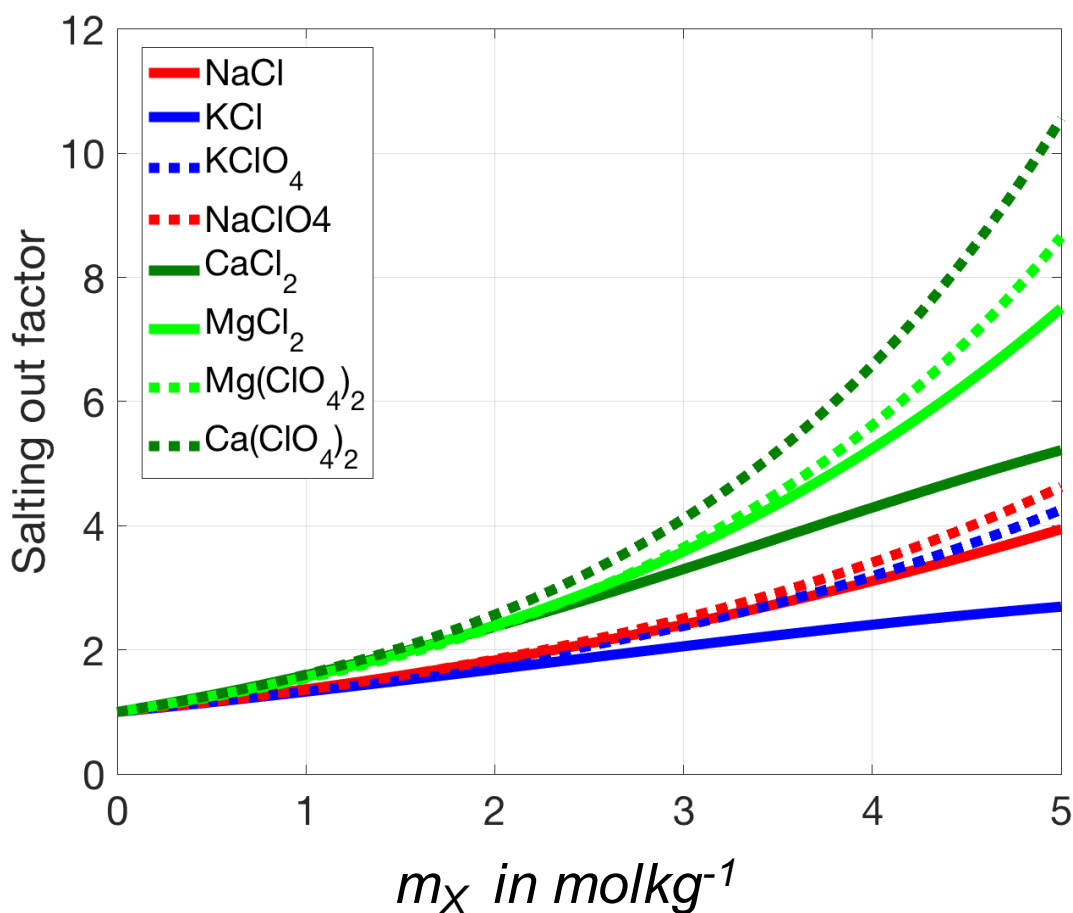


Figure 2S – Salting out coefficients for O_2 in perchlorate and chloride brines: using data on the solubility of O_2 in various chlorides (solid) and perchlorate (dashed) brines¹¹⁻¹³, we computed Pitzer interaction coefficients at 298 K for Ca- and Mg-perchlorates, describing the salting out factor $\gamma_{O_2}(X, m_X)$ of O_2 as a function of salt concentration. We also plotted the salting out factors for other relevant brines (for parameters, see Table 2S).

$[O_2]_{aq,X}(T, P) = \frac{1}{\gamma_{O_2}(X, m_X)} [O_2]_{aq,w}(T, P)$, wherein the salting out factor relates the solubility of O_2 in pure water $[O_2]_{aq,w}(T, P)$ and in the brine $[O_2]_{aq,X}(T, P)$. The salting

out factors for Mg- and Ca-perchlorates are likely overestimated here, as we neglected electrostatic cation-anion-O₂ interactions.

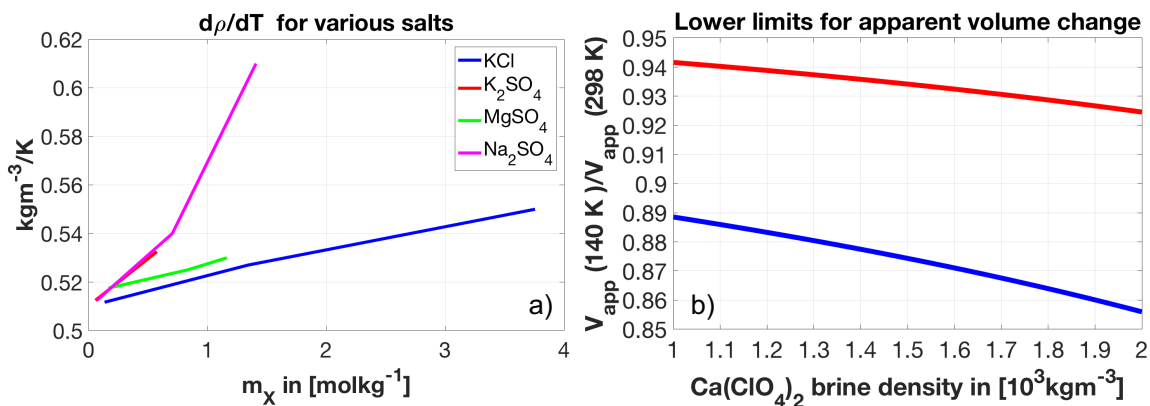


Figure 3S – The temperature dependence of salting out factors for O₂ in various

brines: a) the density gradient with temperature as a function of molality using density data

from 303-243 K. **b)** Using an average density variation from 5-10% for a Ca(ClO₄)₂ brine,

we computed how the apparent volume of water changes from 298-140 K for a range of 4.2

m Ca(ClO₄)₂ brine densities at 298 K (our estimated value is ~1400 kgm⁻³, see below) by

plotting $\frac{V_{app}(\varepsilon \cdot \rho_{brine})}{V_{app}(\rho_{brine})} \approx \frac{V_{app}(140 K)}{V_{app}(298 K)}$, where ε is either 1.05 (red) or 1.1 (blue) (representing

the increase in brine density from 298-140 K by 5-10%). The apparent volume depends

slightly on the reference brine density at 298 K, which we estimated by using Equation

S20, inverting for the brine density and setting approximately $V_{app}(298 K) \approx V_w(298 K)$,

ultimately leading to an estimated 4.2 m Ca(ClO₄)₂ brine density at 298 K of ~1440 kgm⁻³,

and $\frac{V_{app}(\varepsilon \cdot \rho_{brine})}{V_{app}(\rho_{brine})}$ between 0.875 and 0.935. Along the KOH line in the Tromans model³,

we get an increase of the salting out factor between ~3-10 (and likely less than ~5).

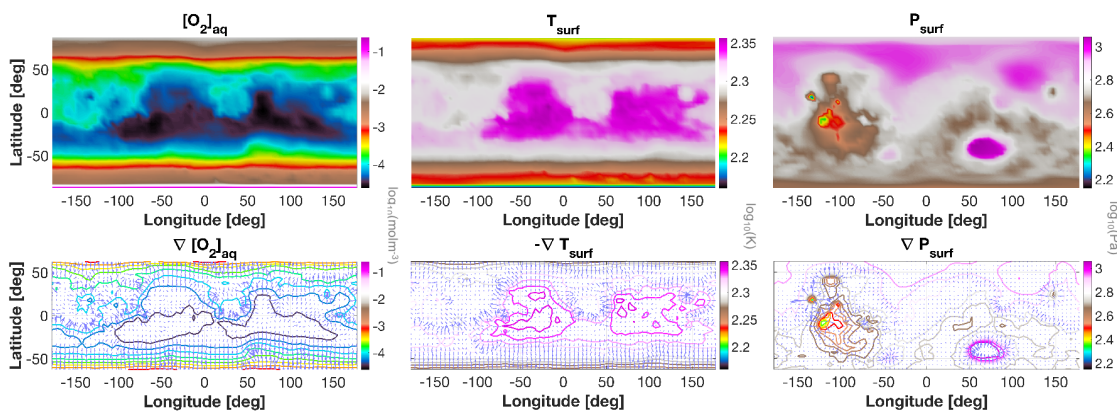


Figure 4S – The predominant factors that control O_2 solubility, and spatial O_2 solubility gradients on modern-day Mars. This plot shows the O_2 solubilities for modern-day Mars using local annual averages for surface temperature and pressure (**top**) as well as spatial gradients (**bottom**) in O_2 solubility. The primary control on O_2 solubility is temperature and secondary modifications result from pressure.

TABLES

Thermodynamic parameters for the solubility of O ₂ in pure water					
Phase of O ₂	$\tilde{\mu}(T_{ref})$ [J mol ⁻¹]	$S(T_{ref})$ [J K ⁻¹ mol ⁻¹]	$C_P(T_{ref})$ [J K ⁻¹ mol ⁻¹]	T_{ref} [K]	P_{ref} [Pa]
Gaseous	0	205.028	29.332	298	1.01325·10 ⁵
Aqueous	16506	109	205.266	298	1.01325·10 ⁵

Table 1S: Lists all thermodynamic parameters needed to compute the specific heat capacity for O₂ at constant pressure in the gaseous and aqueous phases, essential for deriving the solubility of O₂ in pure water as a function of pressure and temperature in Equations 1 and 2. The parameters are taken from experiments¹. The partial volume fraction in the Martian atmosphere is approximately $f_{O_2} = 0.00146^5$, and $R = 8.3144598 \text{ Jmol}^{-1}\text{K}^{-1}$ is the universal gas constant.

Salting-out parameters								
Salt	Ions	f_c	f_a	λ_{O_2-c} [kg mol ⁻¹] [¹]	λ_{O_2-a} [kg mol ⁻¹] [¹]	λ_{O_2-c-a} [kg ² mol ⁻²] [²]	M_X [kg mol ⁻¹] [¹]	V_X [10 ⁻⁶ m ³ mol ⁻¹] [¹]
Ca(ClO ₄) ₂	Ca ²⁺ /ClO ₄ ⁻	1	2	0.2497	-0.007	0	0.23898	90.147
Mg(ClO ₄) ₂	Mg ²⁺ /ClO ₄ ⁻	1	2	0.2298	-0.007	0	0.22321	101
NaClO ₄	Na ⁺ /ClO ₄ ⁻	1	1	0.1602	-0.007	0	0.12244	48.988
KClO ₄	K ⁺ /ClO ₄ ⁻	1	1	0.1519	-0.007	0	0.13855	54.980
MgCl ₂	Mg ²⁺ /Cl ⁻	1	2	0.2298	0	-0.00565	0.09521	40.81
CaCl ₂	Ca ²⁺ /Cl ⁻	1	2	0.2497	0	-0.0169	0.11098	50.5
NaCl	Na ⁺ /Cl ⁻	1	1	0.1602	0	-0.00919	0.05844	27.02
KCl	K ⁺ /Cl ⁻	1	1	0.1519	0	-0.0211	0.07455	37.52
MgSO ₄	Mg ²⁺ /SO ₄ ²⁻	1	1	0.2298	0.0878	0	0.12037	40.7
K ₂ SO ₄	K ⁺ /SO ₄ ²⁻	2	1	0.11519	0.0878	0	0.17426	65.48
Na ₂ SO ₄	Na ⁺ /SO ₄ ²⁻	2	1	0.1602	0.0878	-0.046	0.14204	53.33

Table 2S: Specifies the ions, molality of cations (c) or anions (a) per molality of salt, the Pitzer coefficients λ^{11-13} for the interaction of O₂ molecules with cations (c), anions (a), and cations & anions (c-a), and the crystalline molar mass M_X and volume V_X (values have been taken from experiments³ or computed using data²² with $V_X = M_X/\rho_X$, where ρ_X is the density at 298 K and 1 atm~1.01325 bar) for Ca(ClO₄)₂, Mg(ClO₄)₂, NaClO₄, KClO₄,

MgCl₂, CaCl₂, NaCl, KCl, MgSO₄, K₂SO₄, and Na₂SO₄. The crystal data is only necessary to estimate the temperature dependence of the salting out factor in the SOM.

Melting curve parameters						
Salt	T_{eu} [K]	m_{eu} [mol kg ⁻¹]	p_3 [10 ⁻⁵]	p_2	p_1	p_0
Ca(ClO ₄) ₂	198.2	4.176	-1.0689	0.0069556	-1.5378	119
Mg(ClO ₄) ₂	209.3	3.375	-1.4134	0.0094903	-2.1498	167.22
NaClO ₄	239.2	9.2	-0.6053	0.003012	-0.6241	69.098
MgCl ₂	240.15	2.84	-8.5302	0.063718	-15.911	1330.6
CaCl ₂	224	4	-2.56	0.017736	-4.1378	328.69
NaCl	251.85	5.17	0	0	-0.23877	65.22
MgSO ₄	269.55	1.72	0	0	-0.47778	130.51

Table 3S: Specifies the eutectic temperature T_{eu} , the eutectic salt concentration m_{eu} (in mol salt per kg water), and the parameters used to parameterize the critical concentration for the melting curve with temperature for the salts shown in Figure 1, which are Ca(ClO₄)₂, Mg(ClO₄)₂, NaClO₄, MgCl₂, CaCl₂, NaCl, and MgSO₄. Values are taken from experimental data^{10,32}. The melting curve was defined by $m_X(T) = \sum_{i=0}^3 p_i T^i$, $T > T_{eu}$ and $m_X(T) = m_{eu}$, $T \leq T_{eu}$, and determined with experimental data^{10,14,20,21,32,33}.

Temperature variation on the Martian surface with obliquity			
Obliquity <i>[°]</i>	Minimum annual average <i>[K]</i>	Global annual average <i>[K]</i>	Maximum annual average <i>[K]</i>
5	144.4	205.7	229.7
10	144.5	205.4	229.5
15	149.6	205.0	229.0
20	156.0	204.4	228.3
25	161.8	203.703	227.413
25 (with SPC)	144.2	203.651	227.389
40	172.1	201.6	224.1
60	179.7	198.0	214.4
90	177.2	195.4	208.8

Table 4S – Surface temperatures across obliquities: for the simulated obliquities, the minimum, average, and maximum values on the Martian globe for annually averaged surface temperatures. The annotation “with SPC” is representing modern-day Mars, where a perennial CO₂ cap at the south pole was assumed.

Extended References

- 1 Tromans, D. Temperature and pressure dependent solubility of oxygen in water: a thermodynamic analysis. *Hydrometallurgy* **48**, 327-342 (1998).
- 2 Tromans, D. Oxygen solubility modeling in inorganic solutions: concentration, temperature and pressure effects. *Hydrometallurgy* **50**, 279–296 (1998).
- 3 Tromans, D. Modeling Oxygen Solubility in Water and Electrolyte Solutions. *Ind. Eng. Chem. Res.* **39**, 805-812 (2000).
- 4 Taylor, D. F. Thermodynamic Properties of Metal-Water Systems at Elevated Temperatures. *Journal of The Electrochemical Society* **125**, 808, doi:10.1149/1.2131553 (1978).
- 5 Mahaffy, P. R. *et al.* Abundance and isotopic composition of gases in the martian atmosphere from the Curiosity rover. *Science* **341**, 263-266, doi:10.1126/science.1237966 (2013).
- 6 Chase, M. W. J. *et al.* in *Standard Reference Data Program* Vol. 1.0 (National Institute of Standards and Technology, Gaithersburg, MD 20899, 1986).
- 7 Holten, V., Palmer, J. C., Poole, P. H., Debenedetti, P. G. & Anisimov, M. A. Two-state thermodynamics of the ST2 model for supercooled water. *J Chem Phys* **140**, 104502, doi:10.1063/1.4867287 (2014).
- 8 Holten, V., Bertrand, C. E., Anisimov, M. A. & Sengers, J. V. Thermodynamics of supercooled water. *J Chem Phys* **136**, 094507, doi:10.1063/1.3690497 (2012).

- 9 Archer, D. G. & Carter, R. W. Thermodynamic Properties of the NaCl + H₂O System. 4. Heat Capacities of H₂O and NaCl(aq) in Cold-Stable and Supercooled States. *J. Phys. Chem. B* **104**, 8563-8584 (2000).
- 10 Toner, J. D. & Catling, D. C. Water activities of NaClO₄, Ca(ClO₄)₂, and Mg(ClO₄)₂ brines from experimental heat capacities: Water activity >0.6 below 200K. *Geochimica et Cosmochimica Acta* **181**, 164-174, doi:10.1016/j.gca.2016.03.005 (2016).
- 11 Clegg, S. L. & Brimblecombe, P. The solubility and activity coefficient of oxygen in salt solutions and brines. *Geochimica et Cosmochimica Acta* **54**, 3315-3328 (1990).
- 12 Konnik, E. I. Salting-out and Salting-in of Gaseous Non-electrolytes in Aqueous Solutions of Electrolytes. *Russian Chemical reviews* **46**, 577-588 (1977).
- 13 Khomutov N. E., K. E. I. Solubility of oxygen in aqueous electrolyte solutions. *Russian Journal of Physical Chemistry* **48** (1974).
- 14 Toner, J. D., Catling, D. C. & Light, B. A revised Pitzer model for low-temperature soluble salt assemblages at the Phoenix site, Mars. *Geochimica et Cosmochimica Acta* **166**, 327-343, doi:10.1016/j.gca.2015.06.011 (2015).
- 15 Silvester, L. F. & Pitzer, K. S. Thermodynamics of electrolytes. X. Enthalpy and the effect of temperature on the activity coefficients. *Journal of Solution Chemistry* **7**, 327-337, doi:10.1007/BF00662893 (1978).

- 16 Millero, F. J., Huang, F. & Laferiere, A. L. The solubility of oxygen in the major sea salts and their mixtures at 25°C. *Geochimica et Cosmochimica Acta* **66**, 2349-2359, doi:10.1016/s0016-7037(02)00838-4 (2002).
- 17 Millero, F. J. & Huang, F. Solubility of Oxygen in Aqueous Solutions of KCl, K₂SO₄, and CaCl₂ as a Function of Concentration and Temperature. *Journal of Chemical & Engineering Data* **48**, 1050-1054, doi:10.1021/jc034031w (2003).
- 18 Geng, M. & Duan, Z. Prediction of oxygen solubility in pure water and brines up to high temperatures and pressures. *Geochimica et Cosmochimica Acta* **74**, 5631-5640, doi:10.1016/j.gca.2010.06.034 (2010).
- 19 Weiss, R. F. The solubility of nitrogen, oxygen and argon in water and seawater. *Deep-Sea Research* **17**, 721-735 (1970).
- 20 Toner, J. D., Catling, D. C. & Light, B. The formation of supercooled brines, viscous liquids, and low-temperature perchlorate glasses in aqueous solutions relevant to Mars. *Icarus* **233**, 36-47, doi:10.1016/j.icarus.2014.01.018 (2014).
- 21 Toner, J. D., Catling, D. C. & Light, B. Modeling salt precipitation from brines on Mars: Evaporation versus freezing origin for soil salts. *Icarus* **250**, 451-461, doi:10.1016/j.icarus.2014.12.013 (2015).
- 22 Washburn, E. W. *International Critical Tables of Numerical Data, Physics, Chemistry and Technology*. Vol. 3 54-95 (National Research Council, McGraw-Hill Inc., 1928).

- 23 Washburn, E. W. *International Critical Tables of Numerical Data, Physics, Chemistry and Technology*. Vol. 2 327-328 (National Research Council, McGraw-Hill Inc., 1928).
- 24 Ward, W. R. Climatic variations on Mars: 1. Astronomical theory of insolation. *Journal of Geophysical Research* **79**, 3375-3386, doi:10.1029/JC079i024p03375 (1974).
- 25 Mischna, M. A. On the orbital forcing of Martian water and CO₂ cycles: A general circulation model study with simplified volatile schemes. *Journal of Geophysical Research* **108**, doi:10.1029/2003je002051 (2003).
- 26 Forget, F., Haberle, R. M., Montmessin, F., Levrard, B. & Head, J. W. Formation of Glaciers on Mars by Atmospheric Precipitation at High Obliquity. *Science* **311**, 368-371 (2006).
- 27 Laskar, J. *et al.* Long term evolution and chaotic diffusion of the insolation quantities of Mars. *Icarus* **170**, 343-364, doi:10.1016/j.icarus.2004.04.005 (2004).
- 28 Nair, H., Allen, M., Anbar, A. D., Yung, Y. L. & Clancy, R. T. A Photochemical Model of the Martian Atmosphere. *Icarus* **111**, 124-150, doi:10.1006/icar.1994.1137 (1994).
- 29 Gao, P., Hu, R., Robinson, T. D., Li, C. & Yung, Y. L. Stability of CO₂ atmospheres on desiccated M dwarf exoplanets *The Astrophysical Journal* **806**, 12, doi:10.1088/0004-637X/806/2/249 (2015).

- 30 Hanna, J. C. Hydrological modeling of the Martian crust with application to the pressurization of aquifers. *Journal of Geophysical Research* **110**, doi:10.1029/2004je002330 (2005).
- 31 Fairén, A. G. *et al.* Prime candidate sites for astrobiological exploration through the hydrogeological history of Mars. *Planetary and Space Science* **53**, 1355-1375, doi:10.1016/j.pss.2005.06.007 (2005).
- 32 Li, D. *et al.* Phase diagrams and thermochemical modeling of salt lake brine systems.II. NaCl+H₂O, KCl+H₂O, MgCl₂+H₂O and CaCl₂+H₂O systems. *CALPHAD: Computer Coupling of Phase Diagrams and Thermochemistry* **53**, 78-89, doi:10.1016/j.calphad.2016.03.007 (2016).
- 33 Pestova, O. N., Myund, L. A., Khripun, M. K. & Prigarov, A. V. Polythermal Study of the Systems M(ClO₄)₂-H₂O (M²⁺ = Mg²⁺, Ca²⁺, Sr²⁺, Ba²⁺). *Russian Journal of Applied Chemistry* **78**, 409-413 (2005).